Journal of Materials Chemistry C

PAPER

View Article Online
View Journal | View Issue

Cite this: J. Mater. Chem. C, 2019, 7, 2353

Smart strain sensing organic–inorganic hybrid hydrogels with nano barium ferrite as the cross-linker†

Hongbo Gu, *[a] Hongyuan Zhang,[a] Chao Ma,[a] Hongling Sun,[b] Chuntai Liu,[b] Kun Dai,[b] Jiaoxia Zhang,[cd] Renbo Wei, *[de] Tao Ding*[f] and Zhanhu Guo *[d]

Received 29th October 2018,
Accepted 18th January 2019

DOI: 10.1039/c8tc05448g

rsc.li/materials-c

Regarding artificial intelligence and wearable soft electronics, increasing attention has been dedicated to hydrogel strain sensors. However, traditional hydrogels are insulating and fragile. To obtain a continuous and repeatable electrical signal output upon external stress or strain in a hydrogel, the combination of good mechanical property, good elasticity and high electrical conductivity is demanded. In order to apply hydrogel in the strain sensing field, in this work, a smart, flexible organic–inorganic polyanion polyacrylic acid (PAA) hybrid hydrogel is designed with nano barium ferrite ($BaFe_{12}O_{19}$) as a cross-linker without the addition of any chemically covalent or ionic cross-linkers, exhibiting a high ionic conductivity of 1.22×10^{-2} S cm^{-1}. Due to high porosity as confirmed by scanning electron microscope (SEM), the $BaFe_{12}O_{19}$/PAA hybrid hydrogel demonstrates 100% recoverability and stable piezoresistive sensing performance with negligible hysteresis loops under cyclic compression loading tests compared with the *N*,*N*′-methylene bisacrylamide chemically cross-linked PAA hydrogel. This demonstrates that the $BaFe_{12}O_{19}$/PAA hydrogel is not only favorable to be used as a candidate for strain sensors in soft electronics but also facilitates the evolution of a new generation of flexible, wearable, and human-friendly intelligent devices.

1. Introduction

With the increasing development of wearable, flexible and human-friendly soft electronic devices, the multi-functionality and unique structure of the soft materials for sensors, which can transduce external stimuli (for example, strain, temperature, humidity, pH, *etc.*) into an electrical signal (*i.e.*, resistance and capacitance), are imperatively required.[1] Hydrogels, as soft materials (*vs.* hard and fragile metals, ceramics, and carbon),[2] which is composed of a hydrophilic three-dimensional polymer network and a large amount of water, have been widely employed in biomineralization,[3] biosensors,[4] cell modulating substances,[5] drug release vehicles,[6] tissue engineering scaffolds,[7] and smart electronics due to their excellent biocompatibility arising from their unique soft-wet property.[8] Strain sensors, based on the electrical characteristic change under an external strain,[9] have attracted much more attention in the fields of robotics, wearable consumer electronics, damage detection,[10] human motion detection,[11] personal health monitoring, *etc.*[12] Under exposure to a strain field, the hydrogels should possess both good mechanical property and elasticity as well as high electrical conductivity to supply a continuous and repeatable output electrical signal. However, traditional hydrogels are normally electrically non-conductive and very sensitive to external stress or strain; they also possess a low-stretch property and poor mechanical strength because of irregular chemical cross-linking points and broad distributions of chain length,[13] which severely limit their applications in strain sensing fields.[14] There are very few reports on hydrogel-based strain sensors.[15] In addition, polyacrylamide (PAAm)[16] and polyvinyl alcohol (PVA)[17] have been reported as the polymer matrix of the hydrogel; their intrinsically insulating property makes these polymers have to combine with common electronic conductors such as carbon nanotubes (CNTs), graphene, silver nanowire, or ionic ions

[a] Shanghai Key Lab of Chemical Assessment and Sustainability, School of Chemical Science and Engineering, Tongji University, Shanghai, 200092, China. E-mail: hongbogu2014@tongji.edu.cn
[b] Key Laboratory of Materials Processing and Mold (Zhengzhou University), Ministry of Education; National Engineering Research Center for Advanced Polymer Processing Technology, Zhengzhou University, Zhengzhou, 450002, China
[c] School of Material Science and Engineering, Jiangsu University of Science and Technology, Zhenjiang, Jiangsu, 212003, China
[d] Integrated Composites Laboratory (ICL), Department of Chemical & Biomolecular Engineering, University of Tennessee, Knoxville, Tennessee 37966, USA. E-mail: zguo10@utk.edu
[e] College of Chemistry and Chemical Engineering, Henan University, Kaifeng 475004, P. R. China
[f] Research Branch of Advanced Functional Materials, School of Materials and Energy, University of Electronic Science and Technology of China, Chengdu, 611731, P. R. China

† Electronic supplementary information (ESI) available. See DOI: 10.1039/c8tc05448g

(*e.g.* Na^+, H^+), *etc.* in order to behave as a piezoresistive strain sensor and obtain an electrical signal. In this situation, these common electrically conducting nanomaterials may encounter dispersion problems, which may further affect the electrical transport in a hydrogel, especially during the compression cyclic experiments. Therefore, it is necessary to exploit and fabricate a new hydrogel structure to overcome the aforementioned drawbacks.

Poly(acrylic acid) (PAA), known as a common negatively charged polyelectrolyte due to the presence of carboxylic groups on its polymer backbone, is widely applicable as a functional material to control wettability, adhesion, protein adsorption, and cell or bacteria growth.[18] Generally, as a polyanion, the negatively charged PAA aqueous solution, as well as its hydrogels, are electrically conductive. Particularly, PAA-based hydrogels may favor stable electrical signal output without dispersion problems and could be promising polymer candidates for the preparation of strain sensors. Yet, strain sensing hydrogels based on the PAA polymer matrix has been rarely studied.

Novel nanocomposite (NC) hydrogels, one kind of recently developed hydrogels, have attracted more interest originating from their unique structures consisting of organic polymers and inorganic nanofillers with high mechanical strength.[19,20] Normally, in NC hydrogels, instead of organic cross-linking agents, the nanofillers serve as physical cross-linkers to relax the applied stress and prevent cracks by introducing random conformations into the flexible polymer chains and further improving the mechanical properties of the NC hydrogels. The commonly used inorganic nanofillers include clay nanosheets/ceramic oxides/metals,[21] carbon nanodots, carbon nanotubes, graphene oxide, *etc.*[22] However, due to the scarcity of functional groups on the surface of nanofillers,[23] it is normally necessary to chemically modify the surface of the nanofillers with multi-functional groups such as hydroxyls, carbonyls, and epoxides or to add a small amount of chemically covalent and ionic cross-linkers (*i.e.*, *N*,*N*′-methylene bisacrylamide (MBA)) to form NC hydrogels.[24] Though the reported NC hydrogels exhibit excellent mechanical properties, with the aim of obtaining hydrogel strain sensors with good electrical signal performance, high elasticity is also demanded. Thus, the exploration of novel physical cross-linkers and the fabrication of a new structure of NC hydrogels are still challenging objectives.

Barium ferrite ($BaFe_{12}O_{19}$), as a well-known hexagonal hard magnetic materials, has been widely adopted for high-density recording media, microwave devices, and electromagnetic interference (EMI) shielding[25] due to its large saturation magnetization (M_s, 72 emu g^{-1}), high coercivity (H_c, around 1–5 kOe), excellent chemical stability and corrosion resistivity as well as its high Curie temperature.[26] In coordination chemistry, as the fifth element in group 2 and a rare earth metal, Ba^{2+} cations have the capability of forming a Ba^{2+}–ligand complex.[27] Meanwhile, Fe^{3+} is also capable of creating a transition metal complex. Thus, $BaFe_{12}O_{19}$ is a good candidate as a physical cross-linker in the preparation of NC hydrogels. Nevertheless, there are no reports regarding $BaFe_{12}O_{19}$ nanoparticle-based NC hydrogels for strain sensors.

In this work, a novel electrically conducting polyanion PAA hydrogel with $BaFe_{12}O_{19}$ nanoparticles as the physical cross-linkers for a flexible strain controlled manipulator was prepared by the one-step *in situ* polymerization of acrylic acid in $BaFe_{12}O_{19}$ nanoparticle aqueous suspensions without the addition of any chemically covalent or ionic cross-linkers. The formation of the $BaFe_{12}O_{19}$/PAA hydrogel is related to the coordination chemistry between Ba and Fe elements with the carboxyl groups of the PAA polymer as indicated by the Fourier transform infrared spectroscopy (FT-IR), X-ray diffraction (XRD) analysis, and energy-dispersive X-ray spectroscopy (EDX). The $BaFe_{12}O_{19}$/PAA hybrid hydrogel possesses an obvious porous structure as confirmed by scanning electron microscopy (SEM). Consequently, the $BaFe_{12}O_{19}$/PAA hybrid hydrogel exhibits good mechanical property and cyclic compression property with negligible hysteresis loops and 100% recoverability as well as superior piezoresistive strain sensing behaviour compared with the chemically covalent cross-linked PAA with MBA, in which the electrical signal is obviously decreased with cyclic strain.

2. Experimental

2.1. Materials

Barium nitrate ($Ba(NO_3)_2$, $\geq$99.5%), iron nitrate (nonahydrate) ($Fe(NO_3)_3{\cdot}9H_2O$, $\geq$98.5%), ammonia ($NH_3{\cdot}H_2O$, 25–28 wt%), citric acid ($C_8H_8O_7{\cdot}H_2O$, $\geq$99.5%), ammonium persulfate (APS) ($(NH_4)S_2O_8$, $\geq$98.0%), and *N*,*N*′-methylene bisacrylamide ($C_7H_{10}N_2O_2$, MBA, $\geq$98.0%) were provided by Sinopharm Chemical Company, Inc. Acrylic acid (AA, >99%) was purchased from Shanghai Macklin Biochemical Co., Ltd. Fe_3O_4 nanoparticles with an average size of 20 nm were obtained from Nanjing Emperor Nano Material Co., Ltd. All the chemicals were used as received without any further treatment.

2.2. Fabrication of barium ferrite nanoparticles

Barium ferrite ($BaFe_{12}O_{19}$) nanoparticles were synthesized by a sol–gel and self-propagating combustion method as reported in our previous work.[26] Briefly, the citric acid, $Ba(NO_3)_2$ and $Fe(NO_3)_3$ with a molar ratio of citric acid : $Ba(NO_3)_2$: $Fe(NO_3)_3$ = 13 : 1 : 12 were mixed with 10 mL of deionized water for dissolution. Then, ammonia was dripped to adjust the pH value to around 7. After magnetically stirring at 80 °C for 1–2 h in a water bath, the solution became a sol–gel. This sol–gel was self-ignited at 200–220 °C. Lastly, this precursor was ground in a mortar and pestle and put into a tube furnace to anneal at 900 °C for 10 h to obtain well-crystallized $BaFe_{12}O_{19}$ nanoparticles.

2.3. Preparation of barium ferrite/polyacrylic acid hydrogel

PAA, a water-soluble and biocompatible polymer, has considerable applications in the biomedical fields.[28] Therefore, in this work, PAA was chosen as the polymer matrix of the hydrogel. The $BaFe_{12}O_{19}$/PAA hydrogel was in-situ polymerized by the monomer AA in the aqueous suspension of $BaFe_{12}O_{19}$. The $BaFe_{12}O_{19}$ nanoparticles were firstly dispersed in a beaker containing 100 mL of deionized water and 1.0 g of APS under 20 min sonication. Secondly, the suspension was transferred into a three-neck flask under mechanical stirring and sonication for 1 hour at 25 °C.

Then, with the water bath heated to 70 °C, the AA monomers were added into the above-mixed solution dropwise. Afterward, the reaction was conducted at 70 °C for approximate 1–2 hours until the viscosity of the solution increased obviously. Finally, the mixture was poured into a cylindrical polytetrafluoroethylene (PTFE) mold and kept in an oven at 60 °C for 24 h to produce the $BaFe_{12}O_{19}$/PAA hydrogels. In this work, the $BaFe_{12}O_{19}$/PAA hydrogels with a $BaFe_{12}O_{19}$ loading of 0.1, 0.3, and 0.5 wt% were prepared. In comparison, the PAA hydrogel cross-linked with 0.3 wt% chemical MBA was also prepared using the same procedure, which was indexed as the MBA/PAA hydrogel.

2.4. Characterizations

The microstructures of the $BaFe_{12}O_{19}$ nanoparticles and $BaFe_{12}O_{19}$/PAA hydrogels were observed on a field emission scanning electron microscope (FESEM, Hitachi S-4800 system). A thin gold layer with 3 nm of thickness was sputtered onto the SEM specimens. The SEM measurements for the MBA/PAA hydrogel and $BaFe_{12}O_{19}$/PAA hydrogel were performed after freeze-drying. The elemental mapping was carried out *via* energy-dispersive X-ray spectroscopy (EDX, Hitachi SU8020). The TGA test was performed at a heating rate of 5 °C min^{-1} under an air flow rate of 60 mL min^{-1} from 25 to 800 °C.

Fourier transform infrared spectroscopy (FT-IR, Thermo Scientific, Thermo Nicolet NEXUS with an ATR accessory) in the range from 500 to 4000 cm^{-1} with a resolution of 4 cm^{-1} was used to study the formation mechanism of the $BaFe_{12}O_{19}$/PAA hydrogel. The crystalline structures of the $BaFe_{12}O_{19}$, MBA/PAA hydrogel and $BaFe_{12}O_{19}$/PAA hydrogel were proceeded through X-ray powder diffraction (XRD) analysis using a Bruker AXS D8 Discover diffractometer with GADDS (General Area Detector Diffraction System) manipulation, with a Cu-Kα radiation source filtered with a graphite monochromator (λ = 1.5406 Å).

The ionic conductivity (σ_i) of the hydrogels was determined by electrochemical impedance spectroscopy (EIS) with copper blocking electrodes, using a CHI602E Instrument Potentiostat (Shanghai ChenHua Instrument Co., Ltd) over the frequency range of 100 000 to 0.01 Hz at an amplitude of 0 mV (referring to the open circuit potential). The hydrogel with a thickness of around 5 mm was filled between the mirror-finished copper electrodes.[29] The measurements were carried out at room temperature, and the setup is illustrated in Fig. S5 (ESI†).

For compression testing, cylindrical samples of the as-prepared PAA and $BaFe_{12}O_{19}$/PAA hydrogels with a diameter of 25 mm and a height of 25 mm were used in a unidirectional tensile test machine (Shanghai Xieqiang Instrument Technology Co. Ltd). A crosshead speed of 10 mm min^{-1} was used, and the strain (%) was computed by dividing the jogging displacement with the initial gauge length of 25 mm. The compression strength was obtained by the strain at a deformation of 80%. A schematic of the strain sensing measurement is depicted in Fig. S7 (ESI†). The strain sensing compression tests were carried out *via* a universal testing machine with a 100 N load cell (UTM2203, Shenzhen Suns Technology Stock Co. Ltd, China). For the compression hysteresis experiments, cylindrical hydrogels with a diameter of 18 mm and a height of 10 mm were pressed to a compression strain of 40% with a gage length of 10 mm. The volume resistance was measured on a precision digital resistor (Tektronix, DMM 4050). As shown in Fig. S7 (ESI†), the cylindrical hydrogels were put between two copper tap electrodes. The precision digital resistor coupled with the universal testing machine was connected to a computer to record the strain sensing behavior. The measurements were repeated 3–5 times on different specimens for each sample for accuracy. The relative resistance was indexed by $\Delta R/R_0$, where ΔR denotes the resistance change during the compression testing process, and R_0 represents the initial resistance of the hydrogels. After the compression hysteresis tests, the recovery ratio (T_r) of the hydrogel was calculated by eqn (1):[30]

$$T_r = T_c/T_o. \quad (1)$$

where T_c is the residual strain and T_o is the original strain of the hydrogel.

3. Results and discussion

3.1. Characterization of the nano-$BaFe_{12}O_{19}$ and $BaFe_{12}O_{19}$/PAA hydrogels

Fig. S1 (ESI†) shows the SEM images of the as-prepared $BaFe_{12}O_{19}$ nanoparticles. It can be seen that the $BaFe_{12}O_{19}$ nanoparticles manifest the particulate structure and a smooth surface with an average size of 60–80 nm as estimated from the Nano measure 1.2 software. Fig. 1A shows a photo of the as-prepared cylindrical $BaFe_{12}O_{19}$/PAA hydrogel. As depicted in Fig. 1B and C, the photographs of the $BaFe_{12}O_{19}$/PAA hydrogel clearly display excellent elasticity and toughness, are able to be easily restored to its

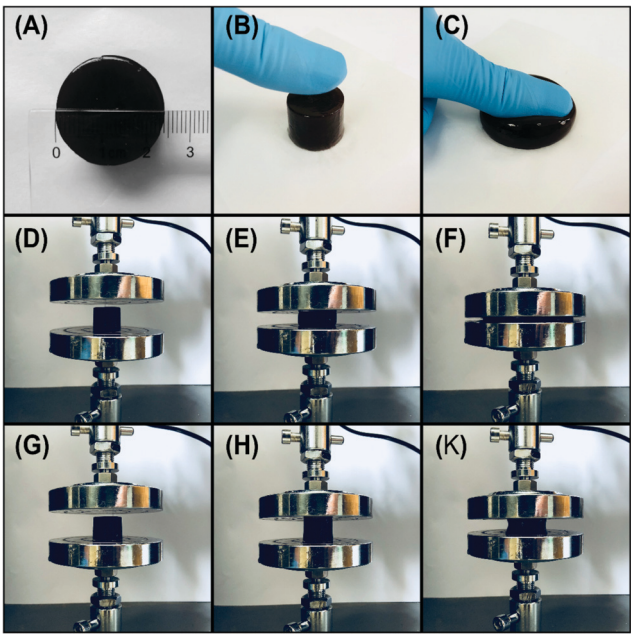

Fig. 1 Photographs of (A) the as-prepared $BaFe_{12}O_{19}$/PAA hydrogel, (B) the $BaFe_{12}O_{19}$/PAA hydrogel before compression, (C) the $BaFe_{12}O_{19}$/PAA hydrogel after compression, (D–F) the compression process of the $BaFe_{12}O_{19}$/PAA hydrogel under a high strain of up to 133 N, and (G–K) the structural recovery after releasing the high strain.

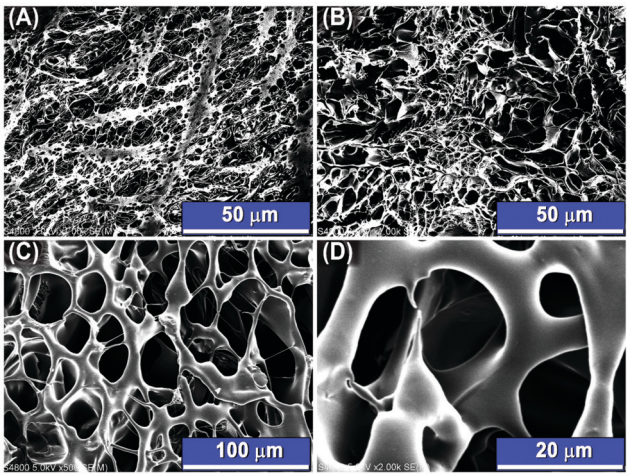

Fig. 2 SEM micrographs for (A) the MBA/PAA and $BaFe_{12}O_{19}$/PAA hydrogels with a $BaFe_{12}O_{19}$ nanoparticle loading of (B) 0.1 wt% and (C) 0.5 wt%, (D) corresponding high magnification for (C) 0.5 wt% $BaFe_{12}O_{19}$ nanoparticle loading of the $BaFe_{12}O_{19}$/PAA hydrogel.

original columnar shape as soon as the stress is removed. Even when the $BaFe_{12}O_{19}$/PAA hydrogels undergo a high strain of 133 N, they recover quickly after the release of the compressive stress without obvious damage (Fig. 1D–F). In order to differentiate MBA/PAA and $BaFe_{12}O_{19}$/PAA hydrogels, the SEM, FT-IR spectra and XRD patterns of the MBA/PAA and $BaFe_{12}O_{19}$/PAA hydrogels were recorded. Fig. 2 shows the SEM images of the MBA/PAA and $BaFe_{12}O_{19}$/PAA hydrogels with different $BaFe_{12}O_{19}$ nanoparticle loadings after freeze-drying. It turns out that the microstructures of both the MBA/PAA and $BaFe_{12}O_{19}$/PAA hydrogels exhibit 3D porous frameworks. Nevertheless, for the MBA/PAA hydrogel, owing to the chemically covalent bonding between MBA and PAA polymer chains, the MBA/PAA hydrogel forms a dense space grid microstructure with different pore sizes (Fig. 2A), which possesses similar morphologies to the hydrogels cross-linked by the common chemically covalent agents.[31] In contrast, the $BaFe_{12}O_{19}$/PAA hydrogels (Fig. 2B–D) reveal a relatively porous structure, corresponding to the formation of a hydrogel matrix,[32] and the pores are noticeably bigger than those of the MBA/PAA hydrogel, especially for the $BaFe_{12}O_{19}$/PAA hydrogels with a $BaFe_{12}O_{19}$ loading of 0.5 wt%. The microstructural differences between these two kinds of hydrogels may lead to different mechanical properties. The highly porous structure of the $BaFe_{12}O_{19}$/PAA hydrogel can provide PAA polymers with sufficient mobility, which may facilitate the rapid response of the hydrogel to external stress/strain.[17]

Fig. 3A shows the FT-IR spectra of $BaFe_{12}O_{19}$, the MBA/PAA hydrogel and the $BaFe_{12}O_{19}$/PAA hydrogel with a $BaFe_{12}O_{19}$ nanoparticle loading of 0.3 wt%. For the as-prepared $BaFe_{12}O_{19}$ nanoparticles, two absorption peaks located at 540 and 575 cm^{-1} can be assigned to the stretching vibrations of the Fe–O[33] and Ba–O bands,[34] respectively. In the FT-IR spectrum of the MBA/PAA hydrogel, the broad peak at around 3332 cm^{-1} is associated with the H–O stretching vibrations.[35] The bands located at 1636 and 1263 cm^{-1} are due to the C=O and C–O stretching vibrations from the carboxylic groups, accordingly. An obvious shoulder peak at around 1700 cm^{-1}, as marked by the rectangle, is due to the C=O stretching vibration from the MBA molecules. Most of these characteristic absorption peaks appear in the

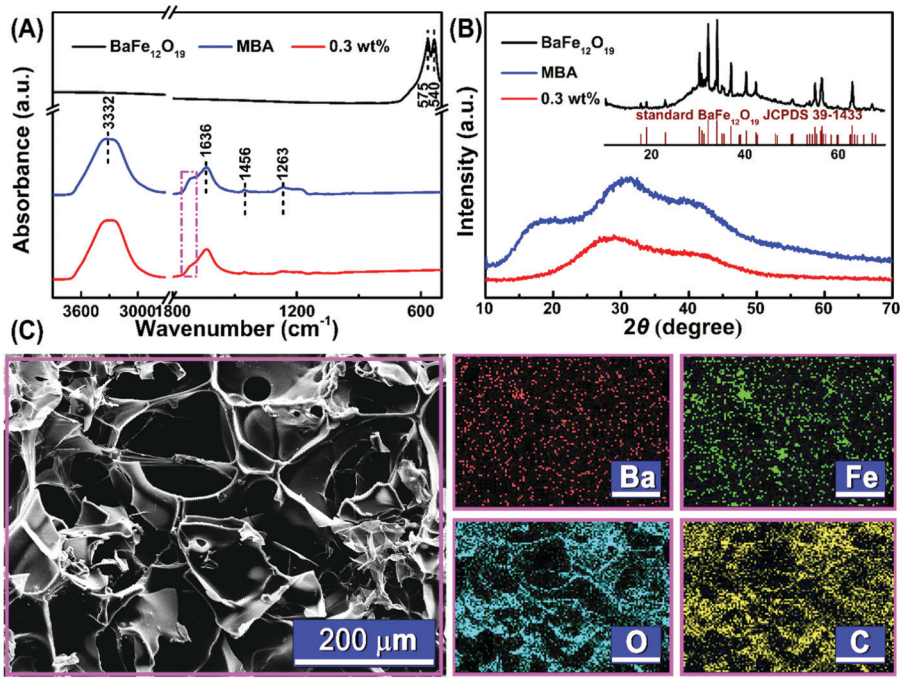

Fig. 3 (A) FT-IR spectra and (B) XRD diffraction patterns of $BaFe_{12}O_{19}$ nanoparticles, MBA/PAA and $BaFe_{12}O_{19}$/PAA hydrogels with a $BaFe_{12}O_{19}$ nanoparticle loading of 0.3 wt%; (C) EDX elemental mapping of $BaFe_{12}O_{19}$/PAA hydrogels with a $BaFe_{12}O_{19}$ nanoparticle loading of 0.3 wt%.

FT-IR spectrum of the $BaFe_{12}O_{19}$/PAA hydrogel, except for the shoulder peak at around 1700 cm^{-1} (which is related to the MBA molecules) as expected. Most importantly, the Fe–O and Ba–O stretching vibrations at around 550 cm^{-1} from the $BaFe_{12}O_{19}$ nanoparticles disappear in the $BaFe_{12}O_{19}$/PAA hydrogel. This may be for the following reasons: this could due to the low $BaFe_{12}O_{19}$ nanoparticle content in the hydrogel (0.3 wt%), or the Ba and Fe elements may have participated in the construction of the $BaFe_{12}O_{19}$/PAA hydrogel since the Ba and Fe atoms exhibit strong coordination ability with the carboxylic groups in PAA.

Fig. 3B shows the XRD diffraction patterns of the as-prepared $BaFe_{12}O_{19}$ nanoparticles, which are consistent with the standard JCPDS No. 39-1433 of typical M type $BaFe_{12}O_{19}$, illustrating the successful preparation of $BaFe_{12}O_{19}$ nanoparticles. Nevertheless, broad peaks are observed in the MBA/PAA and $BaFe_{12}O_{19}$/PAA hydrogels without any evident sharp diffraction peaks. The 2-dimensional elemental distributions in the $BaFe_{12}O_{19}$/PAA hydrogel are clearly shown (Fig. 3C). The zero-loss image of the $BaFe_{12}O_{19}$/PAA hydrogel is shown on the left, and the elemental distributions for Ba, Fe, O, C elements are illustrated on the right. Obviously, Ba and Fe elements are uniformly distributed within the PAA hydrogel matrix, implying that the Ba and Fe elements favour the formation of the PAA hydrogel. Moreover, in order to confirm the contribution of the Ba and Fe elements to the structure of the hydrogel, Fe_3O_4 nanoparticles were used to fabricate the PAA hydrogel for comparison. Unfortunately, the PAA hydrogel cross-linked by Fe_3O_4 nanoparticles cannot be constructed, implying the important role of both the existing Ba and Fe elements in the PAA hydrogel structures. Based on the aforementioned conclusions, both Ba and Fe elements are involved in the construction of PAA hydrogels. The proposed formation mechanism of the $BaFe_{12}O_{19}$/PAA hydrogel is depicted in Scheme 1.

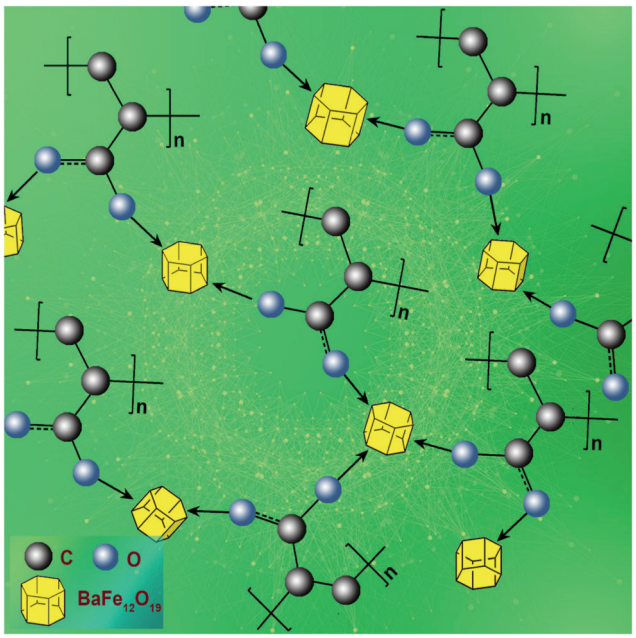

Scheme 1 Proposed formation mechanism of the $BaFe_{12}O_{19}$/PAA hydrogel.

3.2. Ionic conductivity of the $BaFe_{12}O_{19}$/PAA hydrogels

Since the PAA hydrogel is a polyelectrolyte, the electrical conductivity of the PAA hydrogel is dominated by the ionic conductivity (σ_i). The σ_i could be acquired from electrochemical impedance spectroscopy (EIS) measurement through the Nyquist plot (imaginary impedance Z'' *vs.* real impedance Z'). The measured Nyquist plots Z' to $-Z''$ for the MBA/PAA and $BaFe_{12}O_{19}$/PAA hydrogels with a nanoparticle loading of 0.3 wt% are displayed in Fig. 4. Both the MBA/PAA hydrogel and the 0.3 wt% of the $BaFe_{12}O_{19}$/PAA hydrogel show a semicircle in the high-frequency region accompanied by a short line at the low-frequency region as expected. Therefore, the σ_i could be computed from eqn (2):[36]

$$\sigma_i = d/(R_b \times S) \quad (2)$$

where d is the thickness of the hydrogel, S is the area of the hydrogel, and R_b is the resistance of the hydrogels, which could be determined from Z' at a high frequency of 20 kHz. The estimated R_b for the MBA/PAA hydrogel and the 0.3 wt% of the $BaFe_{12}O_{19}$/PAA hydrogel were 27.69 and 26.08 Ω, respectively. The calculated σ_i for the MBA/PAA and $BaFe_{12}O_{19}$/PAA hydrogels were 9.38 and 12.20 mS cm^{-1}, exhibiting a relatively high ionic conductivity.[37]

3.3. Mechanical properties of $BaFe_{12}O_{19}$/PAA hydrogels

Compressibility is a vital characteristic of a material for application in the strain sensing field.[38] Fig. 4A shows the compression stress–strain curves of the MBA/PAA and $BaFe_{12}O_{19}$/PAA hydrogels with different $BaFe_{12}O_{19}$ nanoparticle loadings. All these hydrogels were compressed to 80% for easy comparison. The MBA/PAA hydrogel demonstrates the highest average compression strength up to 130.4 kPa, whereas the average compression strength of the $BaFe_{12}O_{19}$/PAA hydrogels with a $BaFe_{12}O_{19}$ nanoparticle loading of 0.1, 0.3, and 0.5 wt% is 87.1, 65.1, and 23.4 kPa, respectively, Fig. 4B. The compression strength of the $BaFe_{12}O_{19}$/PAA hydrogels is lower than that of the MBA/PAA hydrogel, but the $BaFe_{12}O_{19}$/PAA hydrogels are more flexible than the MBA/PAA hydrogel, since the recovery ratio of the $BaFe_{12}O_{19}$/PAA hydrogels is almost 100% after 10 cycles with 80% compression, exhibiting excellent elasticity. The recovery ratio of the MBA/PAA hydrogel is around 88.5% under the same conditions. For strain sensing application, the recovery ratio of an elastomer is more important for achieving stable electrical signal output.[39] This is consistent with the SEM results shown in Fig. 2. The more porous structures in the $BaFe_{12}O_{19}$/PAA hydrogels (Fig. 2B and C) make the $BaFe_{12}O_{19}$/PAA

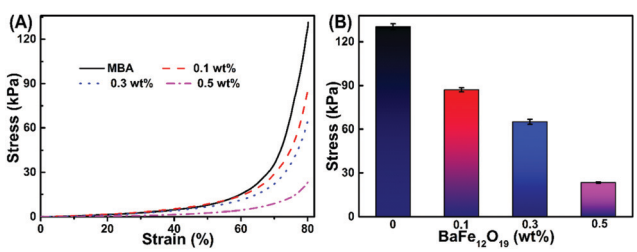

Fig. 4 (A) Compressive stress–strain curves and (B) compressive stresses as a function of $BaFe_{12}O_{19}$ nanoparticle loading at 80% strain.

hydrogels more elastic than the MBA/PAA hydrogel (Fig. 2A), as aforementioned, which is beneficial for their durability under highly compressive forces. Therefore, the $BaFe_{12}O_{19}$/PAA hydrogels can be potentially used as strain sensors. Meanwhile, the compression strength of the $BaFe_{12}O_{19}$/PAA hydrogels is decreased with increasing $BaFe_{12}O_{19}$ nanoparticle loading. This phenomenon is also noticed in the polyacrylamide (PAM)/carbon nanodot (C-dot) NC hydrogels,[22] arising from the fact that the increased $BaFe_{12}O_{19}$ nanoparticle loadings may damage the uniformity of the cross-linked network of the $BaFe_{12}O_{19}$/PAA hydrogels to some extent.

3.4. Strain sensing properties of the $BaFe_{12}O_{19}$/PAA hydrogels

Based on the compression measurements mentioned in Fig. 4, the porous $BaFe_{12}O_{19}$/PAA hydrogel with a $BaFe_{12}O_{19}$ nanoparticle loading of 0.3 wt% was selected to study the strain sensing property of the nanohybrid hydrogel, since it exhibits both strength and flexibility, which favors stable electrical signal output upon compression. In comparison, the MBA/PAA hydrogel was also measured for the same strain sensing test. The strain sensing responsivity is defined as $\Delta R/R_0 = (R - R_0)/R_0$, where R is the resistance after applying compressive stress and R_0 is the initial resistance of the hydrogels. The responsivity as a function of strain up to 40% at a compression rate of 5 mm min^{-1} under cyclic compression for 10 cycles for the MBA/PAA hydrogel and $BaFe_{12}O_{19}$/PAA hydrogels is plotted in Fig. 5A and B, and the corresponding compression stress–strain curves with progressive strain amplitudes (shown in the inset) are depicted in Fig. 5C and D, accordingly. From the electrical response during the compression cycles (Fig. 5A and B), it is observed that the electrical conductivity for both the MBA/PAA and $BaFe_{12}O_{19}$/PAA hydrogels increases with increasing strain (termed as negative piezoresistive behaviour), which is a common phenomenon in piezoresistive materials and results from the formation of additional conductive networks during the compression process.[40] After gradually releasing the stress, the resistance is returned to a high value. This may be related to the elasticity of both the MBA/PAA and $BaFe_{12}O_{19}$/PAA hydrogels, in which the interconnected networks are broken again. However, the electrical signal ($\Delta R/R_0$) for the MBA/PAA hydrogel continues to attenuate over time (Fig. 5A), confirming the non-stable electrical signal output and its harmful effect in regard to strain sensing. By contrast, the $\Delta R/R_0$ exhibits a relatively stable electrical signal output (Fig. 5B), demonstrating that our $BaFe_{12}O_{19}$/PAA hydrogel is more suitable to serve as a strain sensor than the MBA/PAA hydrogel. This might be related to the porous structure of the $BaFe_{12}O_{19}$/PAA hydrogel.

Besides, in order to investigate the sensitivity, stability and reversibility for the 0.3 wt% $BaFe_{12}O_{19}$/PAA hydrogel, the strain sensing behaviours were evaluated for 50 cycles with a compression strain of 40% at a strain rate of 5 mm min^{-1}. The corresponding responsivity variations during cycles of 1–10 and 41–50 are respectively listed in Fig. S4 and S6B (ESI†). The strain sensing behaviour for the 0.3 wt% $BaFe_{12}O_{19}$/PAA hydrogel exhibits a similar profile in all the cycles under stepwise compression. Yet during the first 10 cycles, the $\Delta R/R_0$ is not that stable due to the viscoelasticity of the polymer. With increasing cyclic compression, the construction of perfect and stable conductive networks of $BaFe_{12}O_{19}$/PAA hydrogels endows the hydrogel with a stable electrical signal output.[41] This steady electrical output also indicates the good recoverability and reproducibility of the $BaFe_{12}O_{19}$/PAA hydrogels as strain sensors.

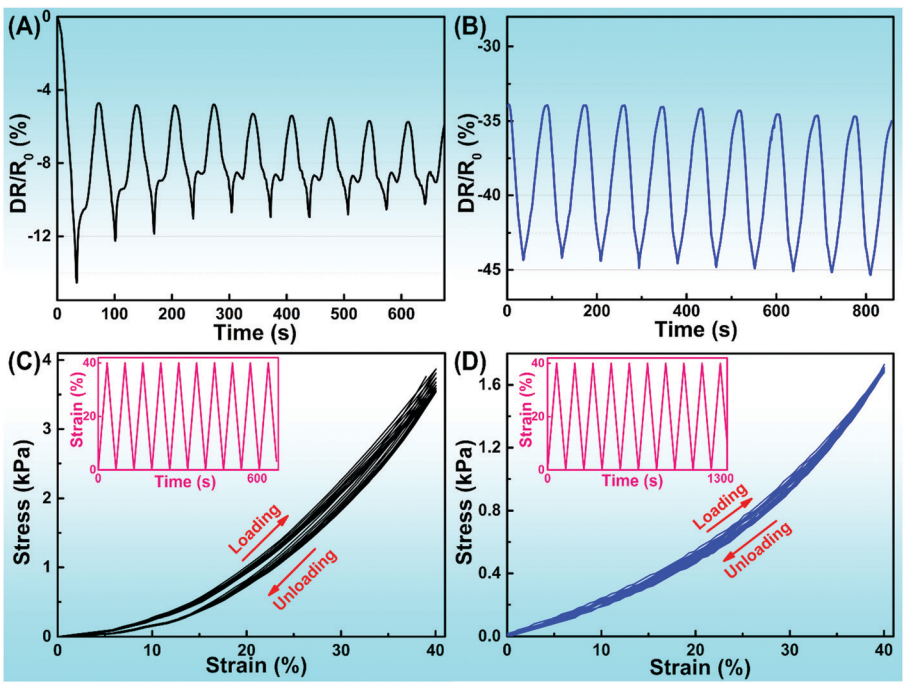

Fig. 5 Strain sensing behavior of (A) the MBA/PAA hydrogel and (B) the $BaFe_{12}O_{19}$/PAA hydrogel with a $BaFe_{12}O_{19}$ nanoparticle loading of 0.3 wt%; and compressive stress–strain curves of (C) the MBA/PAA hydrogel and (D) the $BaFe_{12}O_{19}$/PAA hydrogel with a $BaFe_{12}O_{19}$ nanoparticle loading of 0.3 wt% at up to 40% strain with a strain rate of 5 mm min^{-1}; inset shows the corresponding strain changes over time.

Furthermore, for the MBA/PAA hydrogel, the compression stress–strain curves during the cyclic compression process are clearly separated (Fig. 5C). Both the evidently observed mechanical hysteresis loops (associated with the dissipated energy) and shoulder peaks during the mechanical compression deformation are not suitable for a strain sensor, which are also found in the PAAm hydrogels.[16] In addition, stress–strain curves with negligible hysteresis loops are observed in the $BaFe_{12}O_{19}$/PAA hydrogel (Fig. 5D), which almost fully coincide with all load–unloading compression cycles. A larger hysteresis loop signifies more energy dissipated during the cyclic compression experiments,[41] and the hydrogel possesses lower elasticity with poorer repeatability.[42] This evidences that the $BaFe_{12}O_{19}$/PAA hydrogel has better recoverability and elasticity than the MBA/PAA hydrogel, which affirms that the $BaFe_{12}O_{19}$/PAA hydrogel is more suitable as strain sensing materials than the chemically covalently bonded MBA/PAA hydrogel. This result is consistent with the measured output electrical signal.

4. Conclusion

In summary, this work demonstrates for the first time smart and flexible piezoresistive strain sensing hybrid hydrogels based on the $BaFe_{12}O_{19}$ nanoparticle cross-linked PAA hydrogel without introducing any chemical ingredients such as chemically covalent and ionic cross-linkers. A more stable piezoresistive strain sensing signal is accomplished in the $BaFe_{12}O_{19}$/PAA hybrid hydrogel during the cyclic compression measurements compared with the MBA/PAA hydrogel. This $BaFe_{12}O_{19}$/PAA hybrid hydrogel exhibits excellent recoverability and elasticity arising from its more porous structure as verified by SEM images. The negligible hysteresis loops in the $BaFe_{12}O_{19}$/PAA hybrid hydrogels further affirm the reproducibility and flexibility of this hybrid hydrogel. It is believed that the as-prepared $BaFe_{12}O_{19}$/PAA hybrid hydrogel piezoresistive strain sensors could fulfill the many requirements in stretchable, wearable, flexible and human-friendly soft electronic devices.

Conflicts of interest

There are no conflicts to declare.

Acknowledgements

The authors are grateful for the support and funding from the National Natural Science Foundation of China (No. 51703165), and the Young Elite Scientist Sponsorship Program by CAST (YESS, No. 2016QNRC001). This work is supported by the Shanghai Science and Technology Commission (14DZ2261100).

References

1 (*a*) Z. Lei, Q. Wang, S. Sun, W. Zhu and P. Wu, *Adv. Mater.*, 2017, **29**, 3669–3676; (*b*) G. Liu, Y. Chen, S. Gao, B. Zhang, R. Li and X. Zhuang, *Eng. Sci.*, 2018, **4**, 4–43, DOI: 10.30919/es8d779; (*c*) H. Liu, Q. Li, S. Zhang, R. Yin, X. Liu, Y. He, K. Dai, C. Shan, J. Guo, C. Liu, C. Shen, X. Wang, N. Wang, Z. Wang, R. Wei and Z. Guo, *J. Mater. Chem. C*, 2018, **6**, 12121–12141; (*d*) H. Wei, H. Wang, Y. Xia, D. Cui, Y. Shi, M. Dong, C. Liu, T. Ding, J. Zhang, Y. Ma, N. Wang, Z. Wang, Y. Sun, R. Wei and Z. Guo, *J. Mater. Chem. C*, 2018, **6**, 12446–12467; (*e*) H. Gu, H. Zhang, J. Lin, Q. Shao, D. P. Young, L. Sun, T. D. Shen and Z. Guo, *Polymer*, 2018, **143**, 324–330; (*f*) H. Qi, M. Teng, M. Liu, S. Liu, J. Li, H. Yu, C. Teng, Z. Huang, H. Liu, Q. Shao, A. Umar, T. Ding, Q. Gao and Z. Guo, *J. Colloid Interface Sci.*, 2019, **539**, 332–341; (*g*) D. Y. Choi, M. H. Kim, Y. S. Oh, S.-H. Jung, J. H. Jung, H. J. Sung, H. W. Lee and H. M. Lee, *ACS Appl. Mater. Interfaces*, 2017, **9**, 1770–1780.

2 (*a*) Y. Sheng, J. Yang, F. Wang, L. Liu, H. Liu, C. Yan and Z. Guo, *Appl. Surf. Sci.*, 2019, **465**, 154–163; (*b*) Z. Wang, H. Zhu, N. Cao, R. Du, Y. Liu and G. Zhao, *Mater. Lett.*, 2017, **186**, 274–278; (*c*) Z. Zhao, R. Guan, J. Zhang, Z. Zhao and P. Bai, *Acta Metall. Sin. (Engl. Lett.)*, 2017, **30**, 66–72; (*d*) Z. Zhao, P. Bai1, R. Guan, V. Murugadoss, H. Liu, X. Wang and Z. Guo, *Mater. Sci. Eng., A*, 2018, **734**, 200–209; (*e*) Y. Zhao, L. Qi, Y. Jin, K. Wang, J. Tian and P. Han, *J. Alloys Compd.*, 2015, **647**, 1104–1110; (*f*) Y. Zhao, B. Zhang, H. Hou, W. Chen and M. Wang, *J. Mater. Sci. Technol.*, 2019, DOI: 10.1016/j.jmst.2018.12.009; (*g*) Y. Zhao, S. Deng, H. Liu, J. Zhang, Z. Guo and H. Hou, *Comput. Mater. Sci.*, 2018, **154**, 365–370; (*h*) Y. Zhao, X. Tian, B. Zhao, Y. Sun, H. Guo, M. Dong, H. Liu, X. Wang, Z. Guo, A. Umar and H. Hou, *Sci. Adv. Mater.*, 2018, **10**, 1793–1804; (*i*) C. Wang, V. Murugadoss, J. Kong, Z. He, X. Mai, Q. Shao, Y. Chen, L. Guo, C. Liu, S. Angaiah and Z. Guo, *Carbon*, 2018, **140**, 696–733.

3 R. Xing, K. Liu, T. Jiao, N. Zhang, K. Ma, R. Zhang, Q. Zou, G. Ma and X. Yan, *Adv. Mater.*, 2016, **28**, 3669–3676.

4 P. J. S. King, A. Saiani, E. V. Bichenkova and A. F. Miller, *Chem. Commun.*, 2016, **52**, 6697–6700.

5 D. Seliktar, *Science*, 2012, **336**, 1124.

6 (*a*) R. Reid, M. Sgobba, B. Raveh, G. Rastelli, A. Sali and D. V. Santi, *Macromolecules*, 2015, **48**, 7359–7369; (*b*) S. Li, A. Jasim, W. Zhao, L. Fu, M. W. Ullah, Z. Shi and G. Yang, *ES Mater. Manuf.*, 2018, **1**, 41–49, DOI: 10.30919/esmm5f120.

7 X. Hu, R. Liang, J. Li, Z. Liu and G. Sun, *ES Mater. Manuf.*, 2018, **2**, 16–23.

8 D. Chen, E. Amstad, C.-X. Zhao, L. Cai, J. Fan, Q. Chen, M. Hai, S. Koehler, H. Zhang, F. Liang, Z. Yang and D. A. Weitz, *ACS Nano*, 2017, **11**, 11978–11985.

9 (*a*) M. Amjadi, A. Pichitpajongkit, S. Lee, S. Ryu and I. Park, *ACS Nano*, 2014, **8**, 5154–5163; (*b*) Y. Li, B. Zhou, G. Zheng, X. Liu, T. Li, C. Yan, C. Cheng, K. Dai, C. Liu, C. Shen and Z. Guo, *J. Mater. Chem. C*, 2018, **6**, 2258–2269; (*c*) H. Liu, W. Huang, X. Yang, K. Dai, G. Zheng, C. Liu, C. Shen, X. Yan, J. Guo and Z. Guo, *J. Mater. Chem. C*, 2016, **4**, 4459–4469; (*d*) H. Liu, M. Dong, W. Huang, J. Gao, K. Dai, J. Guo, G. Zheng, C. Liu, C. Shen and Z. Guo, *J. Mater. Chem. C*, 2017, **5**, 73–83.

10 (*a*) N. Wang, Z. Xu, P. Zhan, K. Dai, G. Zheng, C. Liu and C. Shen, *J. Mater. Chem. C*, 2017, **5**, 4408–4418; (*b*) C. Hu,

Z. Li, J. Gao, K. Dai, G. Zheng, C. Liu, C. Shen, H. Song and Z. Guo, *J. Mater. Chem. C*, 2017, **5**, 2318–2328.

11 (*a*) Y. Zheng, Y. Li, Z. Li, Y. Wang, K. Dai, G. Zheng, C. Liu and C. Shen, *Compos. Sci. Technol.*, 2017, **139**, 64–73; (*b*) Y. Lu, M. C. Biswas, Z. Guo, J. Jeon and E. K. Wujcik, *Biosens. Bioelectron.*, 2019, **123**, 167–177.

12 T. Q. Trung and N.-E. Lee, *Adv. Mater.*, 2016, **28**, 4338–4372.

13 Y. Hu, Z. Du, X. Deng, T. Wang, Z. Yang, W. Zhou and C. Wang, *Macromolecules*, 2016, **49**, 5660–5668.

14 L. Qiu, D. Liu, Y. Wang, C. Cheng, K. Zhou, J. Ding, V.-T. Truong and D. Li, *Adv. Mater.*, 2014, **26**, 3333–3337.

15 J. Guo, X. Liu, N. Jiang, A. K. Yetisen, H. Yuk, C. Yang, A. Khademhosseini, X. Zhao and S.-H. Yun, *Adv. Mater.*, 2016, **28**, 10244–10249.

16 J. Y. Sun, C. Keplinger, G. M. Whitesides and Z. Suo, *Adv. Mater.*, 2014, **26**, 7608–7614.

17 (*a*) G. Cai, J. Wang, K. Qian, J. Chen, S. Li and P. S. Lee, *Adv. Sci.*, 2017, **4**, 1600190; (*b*) X. Hu, R. Liang, J. Li, Z. Liu and G. Sun, *ES Mater. Manuf.*, 2018, **2**, 16–23, DOI: 10.30919/esmm5f158; (*c*) S. Li, A. Jasim, W. Zhao, L. Fu, M. W. Ullah, Z. Shi and G. Yang, *ES Mater. Manuf.*, 2018, **1**, 41–49, DOI: 10.30919/esmm5f120.

18 D. Aulich, O. Hoy, I. Luzinov, M. Brücher, R. Hergenröder, E. Bittrich, K.-J. Eichhorn, P. Uhlmann, M. Stamm, N. Esser and K. Hinrichs, *Langmuir*, 2010, **26**, 12926–12932.

19 C. Yao, Z. Liu, C. Yang, W. Wang, X.-J. Ju, R. Xie and L.-Y. Chu, *Adv. Funct. Mater.*, 2015, **25**, 2980–2991.

20 Z. Hu and G. Chen, *Adv. Mater.*, 2014, **26**, 5950–5956.

21 (*a*) M. Liu, Y. Ishida, Y. Ebina, T. Sasaki, T. Hikima, M. Takata and T. Aida, *Nature*, 2014, **517**, 68; (*b*) Z. Zhao, P. Bai, L. Li, J. Li, L. Wu, P. Huo and L. Tan, *Materials*, 2019, **12**, 330; (*c*) Y. Jiao, J. Zhang, S. Liu, Y. Liang, S. Li, H. Zhou and J. Zhang, *Sci. Adv. Mater.*, 2018, **10**, 1706–1713; (*d*) W. Xie, X. Zhu, S. Yi, J. Kuang, H. Cheng, W. Tang and Y. Deng, *Mater. Design*, 2016, **90**, 38–46; (*e*) W. Xie, H. Cheng, Z. Chu, Z. Chen and C. Long, *Ceram. Int.*, 2011, **37**, 1947; (*f*) M. Dong, Q. Li, H. Liu, C. Liu, E. Wujcik, Q. Shao, T. Ding, X. Mai, C. Shen and Z. Guo, *Polymer*, 2018, **158**, 381–390; (*g*) W. Deng, T. Kang, H. Liu, J. Zhang, N. Wang, N. Lu, Y. Ma, A. Umar and Z. Guo, *Sci. Adv. Mater.*, 2018, **10**, 937–949; (*h*) Y. Qian, Y. Yuan, H. Wang, H. Liu, J. Zhang, S. Shi, Z. Guo and N. Wang, *J. Mater. Chem. A*, 2018, **6**, 24676–24685.

22 (*a*) M. Hu, Y. Yang, X. Gu, Y. Hu, Z. Du and C. Wang, *Macromol. Mater. Eng.*, 2015, **300**, 1043–1048; (*b*) T. Su, Q. Shao, Z. Qin, Z. Guo and Z. Wu, *ACS Catal.*, 2018, **8**, 2253–2276; (*c*) H. Gu, H. Zhang, C. Ma, X. Xu, Y. Wang, Z. Wang, R. Wei, H. Liu, C. Liu, Q. Shao, X. Mai and Z. Guo, *Carbon*, 2019, **142**, 131–140; (*d*) L. Wang, H. Qiu, C. Liang, P. Song, Y. Han, Y. Han, J. Gu, J. Kong, D. Pan and Z. Guo, *Carbon*, 2019, **141**, 506–514; (*e*) J. Wang, Z. Shi, X. Wang, X. Mai, R. Fan, H. Liu, X. Wang and Z. Guo, *Eng. Sci.*, 2018, **4**, 79–86, DOI: 10.30919/es8d759; (*f*) H. Du, C. Zhao, J. Lin, Z. Hu, Q. Shao, J. Guo, B. Wang, D. Pan, E. K. Wujcik and Z. Guo, *Chem. Rec.*, 2018, **18**, 1365–1372; (*g*) W. Du, X. Wang, J. Zhan, X. Sun, L. Kang, F. Jiang, X. Zhang, Q. Shao, M. Dong, H. Liu, V. Murugadoss and Z. Guo, *Electrochim. Acta*, 2019, **296**, 907–915.

23 (*a*) H. Gu, C. Ma, J. Gu, J. Guo, X. Yan, J. Huang, Q. Zhang and Z. Guo, *J. Mater. Chem. C*, 2016, **4**, 5890–5906; (*b*) C. Wang, M. Zhao, J. Li, J. Yu, S. Sun, S. Ge, X. Guo, F. Xie, B. Jiang, E. Wujcik, Y. Huang, N. Wang and Z. Guo, *Polymer*, 2017, **131**, 263–271; (*c*) X. Cui, G. Zhu, Y. Pan, Q. Shao, C. Zhao, M. Dong, Y. Zhang and Z. Guo, *Polymer*, 2018, **138**, 203–210; (*d*) Y. He, S. Yang, H. Liu, Q. Shao, Q. Chen, C. Lu, Y. Jiang, C. Liu and Z. Guo, *J. Colloid Interface Sci.*, 2018, **517**, 40–51; (*e*) Z. Wu, H. Cui, L. Chen, D. Jiang, L. Weng, Y. Ma, X. Li, X. Zhang, H. Liu, N. Wang, J. Zhang, Y. Ma, M. Zhang, Y. Huang and Z. Guo, *Compos. Sci. Technol.*, 2018, **164**, 195–203; (*f*) B. Song, T. Wang, H. Sun, H. Liu, X. Mai, X. Wang, L. Wang, N. Wang, Y. Huang and Z. Guo, *Compos. Sci. Technol.*, 2018, **167**, 515–521; (*g*) B. Song, T. Wang, L. Wang, H. Liu, X. Mai, X. Wang, N. Wang, Y. Huang, Y. Ma, Y. Lu, E. K. Wujcik and Z. Guo, *Compos. B*, 2019, **158**, 259–268; (*h*) K. Sun, R. Fan, X. Zhang, Z. Zhang, Z. Shi, N. Wang, P. Xie, Z. Wang, G. Fan, H. Liu, C. Liu, T. Li, C. Yan and Z. Guo, *J. Mater. Chem. C*, 2018, **6**, 2925–2943.

24 Q. Liu, M. Zhang, L. Huang, Y. Li, J. Chen, C. Li and G. Shi, *ACS Nano*, 2015, **9**, 12320–12326.

25 M. Verma, A. P. Singh, P. Sambyal, B. P. Singh, S. K. Dhawan and V. Choudhary, *Phys. Chem. Chem. Phys.*, 2015, **17**, 1610–1618.

26 H. Gu, H. Zhang, C. Ma, S. Lyu, F. Yao, C. Liang, X. Yang, J. Guo, Z. Guo and J. Gu, *J. Phys. Chem. C*, 2017, **121**, 13265–13273.

27 N. S. Poonia and A. V. Bajaj, *Chem. Rev.*, 1979, **79**, 389–445.

28 L. Xiong, T. Yang, Y. Yang, C. Xu and F. Li, *Biomaterials*, 2010, **31**, 7078–7085.

29 A. Noda, K. Hayamizu and M. Watanabe, *J. Phys. Chem. B*, 2001, **105**, 4603–4610.

30 M. Hu, X. Gu, Y. Hu, T. Wang, J. Huang and C. Wang, *Macromolecules*, 2016, **49**, 3174–3183.

31 W. Pu, F. Jiang, P. Chen and B. Wei, *Soft Matter*, 2017, **13**, 5645–5648.

32 Y. Hu, W. Guo, J. S. Kahn, M. A. Aleman-Garcia and I. Willner, *Angew. Chem., Int. Ed.*, 2016, **55**, 4210–4214.

33 H. Gu, H. Lou, J. Tian, S. Liu and Y. Tang, *J. Mater. Chem. A*, 2016, **4**, 10174–10185.

34 J. Zhao, J. Yu, Y. Xie, Z. Le, X. Hong, S. Ci, J. Chen, X. Qing, W. Xie and Z. Wen, *Sci. Rep.*, 2016, **6**, 20496.

35 F. Gao, H. Gu, H. Wang, X. Wang, B. Xiang and Z. Guo, *RSC Adv.*, 2015, **5**, 60208–60219.

36 G. Wee, O. Larsson, M. Srinivasan, M. Berggren, X. Crispin and S. Mhaisalkar, *Adv. Funct. Mater.*, 2010, **20**, 4344–4350.

37 Z. Liu, W. Fu, E. A. Payzant, X. Yu, Z. Wu, N. J. Dudney, J. Kiggans, K. Hong, A. J. Rondinone and C. Liang, *J. Am. Chem. Soc.*, 2013, **135**, 975–978.

38 H. Liu, J. Gao, W. Huang, K. Dai, G. Zheng, C. Liu, C. Shen, X. Yan, J. Guo and Z. Guo, *Nanoscale*, 2016, **8**, 12977–12989.

39 H. Liu, M. Dong, W. Huang, J. Gao, K. Dai, J. Guo, G. Zheng, C. Liu, C. Shen and Z. Guo, *J. Mater. Chem. C*, 2017, **5**, 73–83.

40 L. Qiu, M. Bulut Coskun, Y. Tang, J. Z. Liu, T. Alan, J. Ding, V.-T. Truong and D. Li, *Adv. Mater.*, 2016, **28**, 194–200.

41 H. Deng, M. Ji, D. Yan, S. Fu, L. Duan, M. Zhang and Q. Fu, *J. Mater. Chem. A*, 2014, **2**, 10048–10058.

42 J. Zhang, N. Wang, W. Liu, X. Zhao and W. Lu, *Soft Matter*, 2013, **9**, 6331–6337.

